International Journal of Solids and Structures 51 (2014) 1890–1900

Contents lists available at ScienceDirect

International Journal of Solids and Structures

journal homepage: www.elsevier.com/locate/ijsolstr

Four-point combined DE/FE algorithm for brittle fracture analysis of laminated glass

Wei Xu, Mengyan Zang *

School of Mechanical & Automotive Engineering, South China University of Technology, Guangzhou 510641, People's Republic of China

ARTICLE INFO

Article history:
Received 30 September 2013
Received in revised form 25 January 2014
Available online 21 February 2014

Keywords:
Combined algorithm
Discrete element method
Laminated glass
Averaged stress tensor
Cohesive model

ABSTRACT

A four-point combined DE/FE algorithm is proposed to constrain the rotation of a discrete element about its linked point and analyze the cracks propagation of laminated glass. In this approach, four linked points on a discrete element are combined with four nodes of the corresponding surface of a finite element. The penalty method is implemented to calculate the interface force between the two subdomains, the finite element (FE) and the discrete element (DE) subdomains. The sequential procedure of brittle fracture is described by an extrinsic cohesive fracture model only in the DE subdomain. An averaged stress tensor for granular media, which is automatically symmetrical and invariant by translations, is used to an accurate calculation of the averaged stress of the DE. Two simple cases in the elastic range are given to certify the effectiveness of the combined algorithm and the averaged stress tensor by comparing with the finite element method and the mesh-size dependency of the combined algorithm and the cohesive model is also investigated. Finally, the impact fracture behavior of a laminated glass beam is simulated, and the cracks propagation is compared with experimental results showing that the theory in this work can be used to predict some fracture characteristics of laminated glass.

1. Introduction

Laminated glass has been widely used to enhance the safety of structures, such as automobile windshields, which generally consists of two or more layers of glass sheets combined by adhesive interlayer of tough Polyvinyl Butyral (PVB) under heat treatment. The impact resistance of laminated glass plate is higher than that of a single glass plate of same thickness in total. Simultaneously, the fragments of glass are kept together after broken because of the adhesion of PVB interlayer. The impact fracture behavior of laminated glass is more complicated than that of single glass because of the brittleness of glass, the hyper-elasticity of PVB interlayer and the combined influence of both before. So, many researchers have advocated many numerical methods to study the impact fracture behavior of laminated glass. Among these methods, the finite element method (FEM) (Zienkiewicz et al., 2005) based on continuum mechanics is difficult to simulate the fracture process from the crack growth of glass to the failure of PVB interlayer for laminated glass plate. Peng et al. advanced five laminated windshield FE models and simulated the impact process by using the LS-DYNA software, however, the crack propagation of glass was described by deleting the "glass shell" when it reached failure criterion (Yong et al., 2012). The five FE models were impossible to describe the microscopic behavior in the impact fracture procedure.

The 3D discrete element method (DEM), which is based on non-continuum mechanics as proposed by Cundall (1971) in 1970s, can simulate the fracture behavior of laminated glass (Zang et al., 2007, 2009). In 2009, Shan advanced two sets of spring constants of 3D DE models based on the principle of minimum potential energy and analyzed the stress wave propagation in a concrete block and the splitting process of a marble disc under impact loading (Shan et al., 2009). Recently, the 3D DEM was used to optimize the structure of laminated glass plate by Sakai et al. to improve its impact resistance (Sakai et al., 2013). The validity of the optimum structure was confirmed by the verification analysis. Many contact searching algorithms were developed for a speedier calculation (Munjiza and Andrews, 1998; Williams et al., 2004; Munjiza et al., 2006), however, the poor efficiency of the DEM is the biggest obstacle of its applications in the large scale engineering problems.

To take full advantage of the both numerical methods mentioned before, many kinds of combined DE/FE methods have been advanced to analyze some engineering problems by many scholars.

* Corresponding author. Address: Wushan RD., Tianhe District, Guangzhou 510641, People's Republic of China. Tel.: +86 13922252102; fax: +86 020 87110629.
E-mail addresses: xwteamobj007@gmail.com (W. Xu), myzang@scut.edu.cn (M. Zang).

http://dx.doi.org/10.1016/j.ijsolstr.2014.01.026
0020-7683/

The flexible container problem was considered by using the combined finite-discrete element method (Munjiza, 2004). In this method, each particle was represented by a single DE and each DE was discretized into some FEs. The deformation of individual particles was described by using the continua formulation (FE). The interaction and motion of individual particles was described by using the discontinua formulation (DE). Now, this approach has been widely used to analyze some engineering problems, such as the material fracture behavior (Karami and Stead, 2008), the powder compaction process (Lewis et al., 2005; Gethin et al., 2006; Frenning, 2008; Choi and Gethin, 2009) and the deformable multi-body dynamics (Komodromos and Williams, 2004; Komodromos, 2005). Another popular combined method is a subregional method. For example, Oñate analyzed the rock cutting process by using the subregional combined method, where the tool was discretized with the linear triangle FEs and the rock was discretized with the circle DEs (Oñate and Rojekb, 2004). The failure of a pre-stressed aluminum plate under laser irradiation was simulated. The adjacent region of a failure region was simulated by DEM, and the rest was calculated by FEM (Tang and Xu, 2007; Zhang and Tang, 2010). Lei and Zang proposed a combined algorithm based on penalty method to analyze the impact fracture behavior of a laminated glass plate considering the influence of the model parameters (Lei and Zang, 2010). Afterwards, Yu et al. (2010) and Gao et al. (2014) in Zang's group proposed another two similar combined algorithms to simulate the impact response of a front windshield and the vibration process of the glass plate under impact of a rigid sphere in the elastic range, respectively. Consensus of the three combined algorithms based on penalty method is such that there is only one linked point on the DE combined with one linked point on the corresponding FE surface. The DE may rotate about its linked point and the zero energy mode may be present on the interface. The interface force will vanish when the DE rotates about its linked point.

To constrain the rotation of the DE about its linked point, a four-point combined DE/FE algorithm is proposed to better the computational precision and analyze the cracks propagation of laminated glass. There are four linked points on each DE combined with four nodes of the corresponding FE surface. The interface force is calculated by using the penalty method. The sequential procedure of brittle fracture is described by an extrinsic cohesive fracture model only in the DE subdomain. An averaged stress tensor for granular media, which is automatically symmetrical and invariant by translations, is used to an accurate computation of the averaged stress tensor of the DE. Two simple case in the elastic range are given to validate the effectiveness of the combined algorithm and the averaged stress tensor by comparing with the FEM and the mesh-size dependency of the combined algorithm and the cohesive model is also investigated. Finally, the impact fracture behavior of a laminated glass beam is simulated, and the cracks propagation is compared with the experimental results showing that the theory in this paper can be used to predict some fracture characteristics of the laminated glass.

2. Basic theories of the discrete element model

The first two parts of this section give an introduction about the kinematic formulation and the spring constants of the DE model which are followed by the extrinsic cohesive fracture model and the averaged stress tensor of the DE.

2.1. The kinematic formulation of the DE model

In the DE model, there are many rigid sphere elements (discrete elements). The forces and the moments acting on each DE are given by the second Newton's law. The response of the whole system is described through the interaction of each DE with its neighbouring DEs in the system. The kinematic formulation for the discrete element i can be represented as (Zang et al., 2007):

$$\begin{cases} m_i \ddot{\boldsymbol{a}}_i = \sum_{n=1}^{N_i} \boldsymbol{f}_{in} + \boldsymbol{R}_i \\ I_i \dot{\boldsymbol{\omega}}_i = \sum_{n=1}^{N_i} \boldsymbol{r}_{in} \times \boldsymbol{f}_{in} + \boldsymbol{K}_i \end{cases} \tag{1}$$

where N_i is the number of neighbouring DEs of the element i; m_i and I_i are the mass and the rotary inertia of the element i, respectively; $\boldsymbol{a}_i$ is the displacement of the element i; $\boldsymbol{\omega}_i$ is the rotational velocity of the element i around its center; $\boldsymbol{f}_{in}$ is the force acting on the element i by its neighbouring discrete element n; $\boldsymbol{r}_{in}$ is the arm of the force to the center of the element i; $\boldsymbol{R}_i$ and $\boldsymbol{K}_i$ are the external force and the moment acting on the element i, respectively.

2.2. The spring constants of the twenty-seven spheres DE model

A twenty-seven spheres DE model (Shan et al., 2009) is used to analyze the cracks propagation of laminated glass. As shown in Fig. 1, there are three kinds of DEs (spheres) connecting with the discrete element i (black sphere). The discrete element i is connected with the discrete element j by one normal spring k_n and two tangential springs k_s. The red spheres (such as j_1) are the discrete elements of the first kind, the greens (such as j_2) the second kind and the yellows (such as j_3) the third kind. The relationship between the spring constants and the linear elastic constants had been established based on the strain energy equivalence of elastic body with the elastic potential energy of all the normal and tangential springs (Shan et al., 2009). For the linear elastic material, the normal and the tangential spring constants of the twenty-seven spheres DE model can be represented as follows:

$$\begin{cases} k_{n1} = \frac{E(1-v)}{12r^2(1+v)(1-2v)} V \\ k_{n2} = \frac{E(1+2v)}{12r^2(1+v)(1-2v)} V \\ k_{s1} = k_{s2} = \frac{E(1-4v)}{12r^2(1+v)(1-2v)} V \\ k_{n3} = k_{s3} = 0 \end{cases} \tag{2}$$

where k_{n1}, k_{n2} and k_{n3} represent the normal spring constants between the discrete element i and its three kinds of the connective DEs (such as j_1, j_2 and j_3), respectively; k_{s1}, k_{s2} and k_{s3} represent the tangential spring constants between the discrete element i and its three kinds of the connective DEs respectively; v is Poissons ratio; E is Young's modulus; V is the volume of the DE and r is the radius of the DE; The volume is $V = 8r^3$ for the twenty-seven spheres DE model.

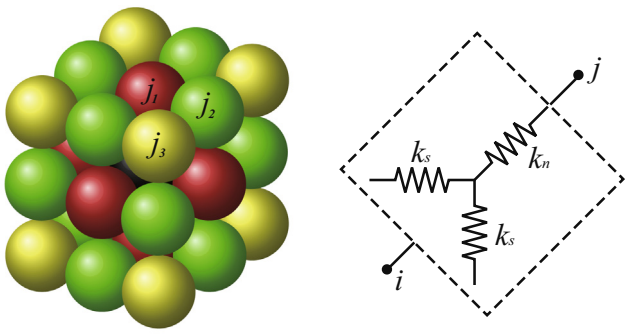

Fig. 1. Twenty-seven spheres discrete element model.

2.3. The extrinsic cohesive fracture model

Particularly for the brittle material, such as glass and ceramic, the essence of its brittle fracture can be sought at the atomic or molecular level (Lawn, 1993). To describe the sequential picture of brittle fracture, the extrinsic cohesive fracture model is added between the two joint models of the DE, the connective model and the contact model (Gao and Zang, 2013).

The effective quantities gives the basis of the extrinsic cohesive fracture model which integrate the effective traction and the effective separation between the neighboring elements (Ortiz and Pandolfi, 1999; Zhang et al., 2007). The relationship between the effective cohesive traction and the effective separation, as shown in Fig. 2, can be represented as:

$$f_n = \sigma_{eff}^n A = \sigma_c \delta_n A \left(\frac{\delta_{eff}}{\delta_{eff}^{\max}} - \frac{\delta_{eff}}{\delta_c} \right) \Big/ \delta_{eff}^{\max} \tag{3}$$

$$f_s = \sigma_{eff}^s A = \eta \sigma_c \delta_s A \left(\frac{\delta_{eff}}{\delta_{eff}^{\max}} - \frac{\delta_{eff}}{\delta_c} \right) \Big/ \delta_{eff}^{\max} \tag{4}$$

where f_n and f_s are the normal and the tangential forces respectively, and the two components of the tangential force are:

$$f_{s1} = f_s u_{s2} / u_s \tag{5}$$

$$f_{s2} = f_s u_{s3} / u_s \tag{6}$$

here u_{s2}, u_{s3} and u_s are two tangential displacements and the sum of the tangential displacement respectively; δ_c is the critical separation; δ_n and δ_s are the normal separation and the tangential separation, respectively; η is the shear stress factor; $\delta_{eff}^{\max}$ is the max effective separation until current time from the initial moment; δ_{eff} is the effective separation at current time; A is the equivalent area between the DEs.

The effective separation δ_{eff} at current time can be obtained from the following formulas:

$$\delta_{eff} = \begin{cases} \sqrt{\delta_n^2 + (\eta \delta_s)^2}, & \sigma_{eff}^n > 0 \\ \eta |\delta_s|, & \sigma_{eff}^n \leqslant 0 \end{cases} \tag{7}$$

2.4. The averaged stress tensor of the discrete element

An averaged stress tensor, which was automatically symmetrical and invariant by translations, was developed by Fortin for granular media (Fortin et al., 2003; de Saxcé et al., 2004). The averaged stress of each granular is calculated by:

$$\sigma = \frac{1}{V} \int_V \boldsymbol{r} (\rho \boldsymbol{g})^t - \frac{1}{V} \int_V \boldsymbol{r} (\rho \ddot{\boldsymbol{u}})^t + \frac{1}{V} \boldsymbol{r} \boldsymbol{f}_c^t \tag{8}$$

in which V is the volume of granular; $\boldsymbol{r}$ denotes the position vector of a current point of the granular; ρ is the density; $\boldsymbol{g}$ is the gravity acceleration; $\boldsymbol{u}$ is the displacement vector of a current point of the granular; $\boldsymbol{f}_c$ is the contact force acting on the granular. The three items in the right hand side denote the stress components contributing to gravity, inertia force and contact force, respectively.

In order to calculate the averaged stress of the DE, the contribution of connect force, cohesive traction and interface force between the DEs to the stress components are subjoined in Eq. (8), and the stress component owing to the gravity vanishes by taking the mass center of the DE as origin. So the averaged stress of the DE can be obtained by:

$$\sigma = -\frac{1}{V} \int_V \boldsymbol{r} (\rho \ddot{\boldsymbol{u}})^t + \frac{1}{V} \boldsymbol{r} \boldsymbol{f}_c^t + \frac{1}{V} \boldsymbol{r} \boldsymbol{f}_n^t + \frac{1}{V} \boldsymbol{r} \boldsymbol{f}_v^t + \frac{1}{V} \boldsymbol{r} \boldsymbol{f}_i^t \tag{9}$$

in which $\boldsymbol{f}_n, \boldsymbol{f}_v$ and $\boldsymbol{f}_i$ denote the connect force, the cohesive traction and the interface force acting on the DE, respectively.

Remark. The external force acting on the center of the DE is regarded as the contact force. The position of the acting point is on the spherical surface of the DE and keeps the same as the initial time.

3. The four-point combined DE/FE algorithm

The first part of this section gives the weak form of the system governing equation. The second part presents the four-point combined algorithm followed by the interface force calculation and time step.

3.1. The weak form of the system governing equation

A continuous 3D elastic solid (solution domain) is considered with the volume Ω and the surface S as shown in Fig. 3. The elastic solid is divided into two subdomains, Ω_a and Ω_b with the surfaces $S_{\sigma a}, S_{ua}$ and $S_{\sigma b}, S_{ub}$, respectively, which are to be joined together along an interface S_{ab}. Here $S_{\sigma a}$ and $S_{\sigma b}$ are the surfaces prescribed the external forces, S_{ua} and S_{ub} are the surfaces prescribed the displacements (Lei and Zang, 2010). In this work the solution domain is decomposed into the DE and FE subregions which are combined with the four-point combined DE/FE algorithm based on the penalty method presented detailed later.

Based on the theory of the solid mechanics the combined DE/FE algorithm is equivalent to solving the conditional stationary value of functional. The functional is given by the following formula:

$$\Pi_p = \Pi_{pa} + \Pi_{pb} \tag{10}$$

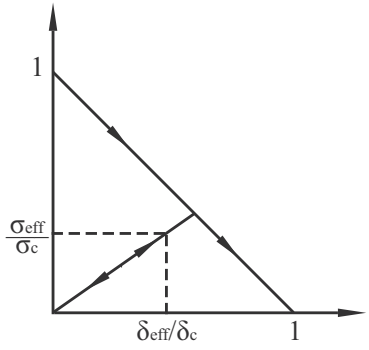

Fig. 2. The relationship between the effective traction σ_{eff} and the separation δ_{eff}.

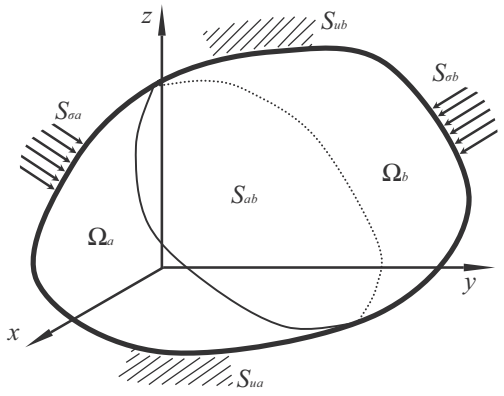

Fig. 3. Solution domain divided into two subdomains.

in which Π_{pa} and Π_{pb} are the functionals that are related to displacement u_i^a and u_i^b respectively, here u_i^a and u_i^b are the displacement functions in the subregion a and b. The kinematics condition restrains the displacements of the points on the interface S_{ab} of the two subdomains to satisfy the impenetrability:

$$u_i^a - u_i^b = 0 \tag{11}$$

In this work the product of the kinematics condition is introduced to the functional in Eq. (10) by using the penalty method:

$$\Pi_p^* = \Pi_p^*(u_i^a, u_i^b) = \Pi_{pa} + \Pi_{pb} + \int_{S_{ab}} \frac{\alpha}{2}(u_i^a - u_i^b)^2 dS \tag{12}$$

where α is the penalty factor and is close to $+\infty$.

The first variation of Π_p^* is:

$$\delta\Pi_p^* = \delta\Pi_{pa} + \delta\Pi_{pb} + \int_{S_{ab}} \alpha(u_i^a - u_i^b)(\delta u_i^a - \delta u_i^b) dS \tag{13}$$

in which

$$\delta\Pi_{pa} = \int_{\Omega_a} \left[\sigma_{ij}\delta u_{i,j}^a - (\bar{f}_i - c\dot{u}_i^a - \rho\ddot{u}_i^a)\delta u_i^a\right] d\Omega - \int_{S_{\sigma_a}} \bar{p}_i \delta u_i^a dS \tag{14a}$$

$$\delta\Pi_{pb} = \int_{\Omega_b} \left[\sigma_{ij}\delta u_{i,j}^b - (\bar{f}_i - c\dot{u}_i^b - \rho\ddot{u}_i^b)\delta u_i^b\right] d\Omega - \int_{S_{\sigma_b}} \bar{p}_i \delta u_i^b dS \tag{14b}$$

Here, σ_{ij} is a component of the Cauchy stress tensor; $\bar{f}_i$ and $\bar{p}_i$ are the body force per unit volume and the boundary tractions per unit area respectively; c and ρ are the damping coefficient and the material density. Because of the independence of u_i^a and u_i^b, $\delta\Pi_p^* = 0$ can be decomposed:

$$\delta\Pi_{pa} + \int_{S_{ab}} \alpha(u_i^a - u_i^b)\delta u_i^a dS = 0 \tag{15a}$$

$$\delta\Pi_{pb} - \int_{S_{ab}} \alpha(u_i^a - u_i^b)\delta u_i^b dS = 0 \tag{15b}$$

Eqs. (15a) and (15b) are the weak forms of the system governing equations for the subdomains a and b, respectively. According to the principle of virtual displacement, it is obvious that the item $\alpha(u_i^a - u_i^b)$ in Eq. (15) is the stress acting on the interface S_{ab}.

3.2. The four-point combined DE/FE algorithm

As illustrated in Fig. 4, there are three typical combined DE/FE algorithms, which are the nodal combined algorithm (Lei and Zang, 2010), the surface-center combined algorithm (Yu et al., 2010) and the freely combined algorithm (Gao et al., 2014), developed by researchers in Zang's group.

For the nodal combined algorithm, there are four discrete elements D_1, D_2, D_3 and D_4 combined with the four nodes N_1, N_2, N_3 and N_4 of the finite element F, respectively, the linked points L_1, L_2, L_3 and L_4 on the DE are coincident with the four nodes at the initial moment respectively; for the surface-center combined algorithm, there is one discrete element D combined with a surface $N_1N_2N_3N_4$ of the finite element F, the linked point L_1 is just located at the surface center; for the freely combined algorithm, the discrete element D is combined with the surface $N_1N_2N_3N_4$ of the finite element F, the linked point L_1 may be located at any point of the surface. For these combined DE/FE algorithms, there is only one linked point on the DE combined with the corresponding FE surface. The DE may rotate about its linked point and the zero energy mode may be present on the interface. The interface force will vanish between the DE and FE subregions when the DE rotates about its linked point.

In order to constrain the rotation of the DE about its linked point and eliminate the zero energy mode on the interface, we propose a four-point combined DE/FE algorithm. As shown in Fig. 5, the discrete element D is combined with the square surface $N_1N_2N_3N_4$ of the finite element F. The linked points $L_i (i = 1, 2, 3, 4)$ on the discrete element D coincide with the nodes N_i of the finite element F at the initial moment, respectively. The displacement constraint between the discrete element D and the finite element F is imposed on the linked points L_i and the nodes N_i based on the penalty method. So it is impossible for the discrete element D to rotate about its linked points.

For an elastic solid, the brittle fracture is processing only in the DE subdomain. Taking account of the spatial arrangement of discrete elements as shown in Fig. 1, the artificial interface between the DE and FE subdomain should be a plane or a collection of some planes, such as the interfaces of the glass beam and the laminated glass beam in the later Section 4. An artificial interface of the arbitrary geometry can be constructed for the four-point combined DE/FE algorithm. As a simple example of a 2D arbitrary geometry, the interface of an elliptic subdomain in a square plane is illustrated in Fig. 6. The interface (the green polyline) between the DE and FE subdomain tends to the red ellipse (the real boundary between two subdomains) if the size of the DEs is small enough.

Remark. For the four-point combined DE/FE algorithm the FE surface on the interface should be square. Yet the DE is not limited to combine with the four nodes of the FE surface. The linked point on the FE is not always the node of the FE surface and may be any point on the FE surface. One DE may be combined with some FE surfaces and one FE surface may be combined with some DEs. Because the interface stiffness tends to infinity, the deformation of the FE surface on the interface is constrained. However, the error of the simulation result can be neglected for the small deformation problems.

3.3. The interface force calculation

The essence of the combined DE/FE algorithm is the imposition of the displacement constraint on the interface. It is finished by acting the displacement constraint on some discrete points (linked

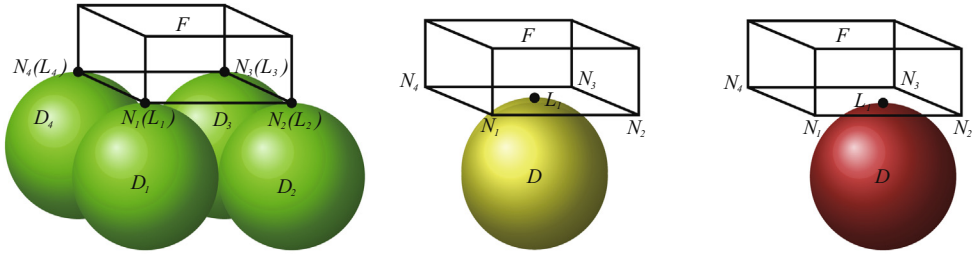

(a) Nodal combined algorithm (b) Surface-center algorithm (c) Freely combined algorithm

Fig. 4. The three combined DE/FE algorithms.

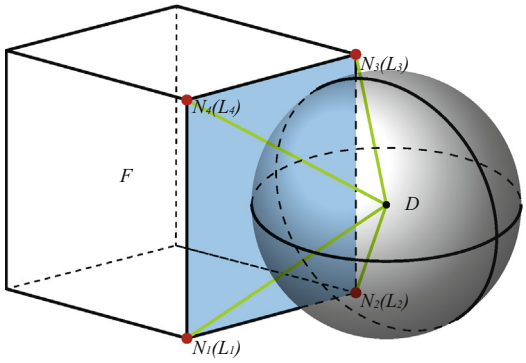

Fig. 5. The four-point combined DE/FE algorithm.

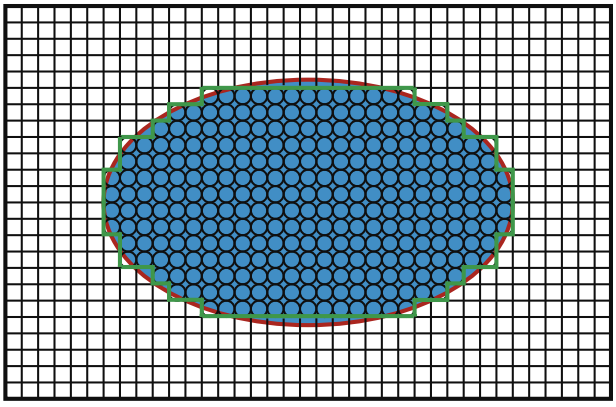

Fig. 6. The interface construction of an elliptic subdomain.

points) of the DE and FE on the interface by the penalty method. Hence, the second item of Eq. (15a) and/or (15b), the interface force, can be calculated by the following equation in a matrix form:

$$\int_{S_{ab}} \alpha(u_i^a - u_i^b)\delta u_i^a dS = \sum_e \delta \boldsymbol{u}^{e\top} \boldsymbol{K}_c^e \Delta \boldsymbol{u}^e \tag{16}$$

where,

$$\boldsymbol{K}_c^e = \int_{S_{ab}^e} \boldsymbol{N}^\top \boldsymbol{\alpha} \boldsymbol{N} dS$$

is the interface stiffness matrix, in which $\boldsymbol{\alpha}$ is matrix of the penalty factor, and $\boldsymbol{N}$ is a matrix of shape functions for the nodes in the FE; $\Delta \boldsymbol{u}^e = \boldsymbol{u}^n - \boldsymbol{u}^l$ is a vector of the relative displacement between nodes in the FE subregion and their corresponding linking points in the DE subregion. Here, $\boldsymbol{u}^n$ and $\boldsymbol{u}^l$ are the vectors of the displacement of nodes and their linking points respectively.

After some simple mathematical operations, the interface force in Eq. (16) may be calculated by the following simple formula:

$$\int_{S_{ab}} \alpha(u_i^a - u_i^b)\delta u_i^a dS = K_c \sum_e (\delta \boldsymbol{u}^{e\top} \Delta \boldsymbol{u}^e) \tag{17}$$

where $K_c = \gamma K r^2$ is the interface stiffness, in which γ is the scale factor; $K = min(K_d, K_f)$, in which $K_d = E_d/(1-2\mu_d), K_f = E_f/(1-2\mu_f)$, and E_d and E_f are Young's modulus of the DE and FE subregion respectively, μ_d and μ_f are Poissons ratio of the DE and FE subregion, respectively; the penalty factor α is set to be $\alpha = \gamma K$ in the numerical simulations. The detailed procedures of the interface force calculation are given by the following part of this section.

As shown in Fig. 5 the displacement of the linked point L_i (i = 1, 2, 3 and 4) on the DE can be obtained by:

$$\boldsymbol{u}_i^l = \boldsymbol{u}^d + \boldsymbol{u}_r^d \tag{18}$$

in which $\boldsymbol{u}^d$ is the translational displacement of the DE center; $\boldsymbol{u}_r^d$ is the relative displacement between the linked point L_i and the DE center. The displacement of the linked point on the FE surface is the displacement of the corresponding node, $\boldsymbol{u}_i^n$.

After obtained the displacements of the two linked points, the interface force acting on the linked point L_i can be calculated by the following formula:

$$\boldsymbol{f}_i^d = K_c \boldsymbol{\delta} \tag{19}$$

in which $\boldsymbol{\delta} = \boldsymbol{u}_i^n - \boldsymbol{u}_i^l$ is the penetration or separation vector between the linked point L_i on the DE and the node N_i of the corresponding FE surface.

The interface force acting on the linked point L_i is equivalent to a force $\boldsymbol{F}_i^d$ and a moment $\boldsymbol{M}_i^d$ acting on the DE, in which the force $\boldsymbol{F}_i^d = \boldsymbol{f}_i^d$ and the moment $\boldsymbol{M}_i^d$ is calculated by the following formula:

$$\boldsymbol{M}_i^d = \boldsymbol{r}_i^d \times \boldsymbol{f}_i^d \tag{20}$$

here, $\boldsymbol{r}_i^d$ is the arm of the interface force $\boldsymbol{f}_i^d$ to the DE center.

The interface force acting on the linked point N_i (node) of the FE surface equals and opposites to the force acting on the linked point L_i:

$$\boldsymbol{f}_i^n = -\boldsymbol{f}_i^d \tag{21}$$

3.4. Time step

Since the Central Difference Method, which is conditionally convergent, is employed in the four-point combined algorithm, the time step must satisfies the numerical stability conditions. According to the physical theory, the momentum transferring from one body to the other in a single time step Δt should not exceed the total momentum exchanging during a two-body collision process (Lei and Zang, 2010). So the critical time step Δt_{cr} in the combined model may be given by:

$$\Delta t_{cr} \leqslant \min\{\Delta t_{dcr}, \Delta t_{ccr}, \Delta t_{fcr}\} \tag{22}$$

in which,

$$\Delta t_{dcr} = \sqrt{\frac{m^d}{k_n}} \tag{23}$$

is the critical time step in the DE subdomain, here m^d and k_n are the mass of the DE and the normal stiffness between DEs;

$$\Delta t_{ccr} = \min_{i,j} \sqrt{\frac{2 m_i^n m_j^d}{n_i k_c (m_i^n + m_j^d)}} \tag{24}$$

is the critical time step determined by the DEs and the nodes near the interface S_{ab}, here m_i^n is the mass of node i; n_i is the number of FEs which contain node i;

$$\Delta t_{fcr} = \frac{L_{min}}{C_f} \tag{25}$$

is the critical time step in the FE subregion, here L_{min} is the minimum effective length of FEs, $C_f = \sqrt{E_f(1-\mu_f)/[\rho_f(1+\mu_f)(1-2\mu_f)]}$ is the velocity of elastic wave, and ρ_f is the density of material in the FE subregion.

4. Numerical test

4.1. The vibration of the cantilever beam under impact load

To investigate the influence of the penalty factor α on the simulation results, the four-point combined DE/FE algorithm is used to simulate the vibration of a cantilever beam under impact load and the simulation results with different scale factors γ are compared with that of the FEM. The cantilever beam is illustrated in Fig. 7. The size of the cantilever beam, which is subjected to a dynamic load at the place 2.0 mm apart from the right end (the free end, and the left end fixed), is 120 mm × 12 mm × 20 mm. The load, whose maximum total force is 147 N and rise time is $t_0 = 2.0$ ms (shown in Fig. 8), is uniformly distributed on the surface of the beam. The material constants of the cantilever beam are: Young's modulus E = 74.09 GPa, Poisson's ratio $\mu = 0.2$, and density $\rho = 2500\ \mathrm{kg/m^3}$.

As one of the important parameters of the penalty method, the scale factor γ in Eq. (17) or Eq. (19) influences the simulation results. In this work, the difference between the simulation results calculated by the four-point combined method with different scale factors is considered. The cantilever beam is discretized into 4800 DEs with the radius of 0.5 mm (the blue subregion as shown in Fig. 7 and 24,000 cubic FEs with the size of 1 mm. Fig. 9 shows the deflection (displacement in the y direction) at point A on the right free end. It shows that, when a large enough scale factor γ is set, the results calculated by the four-point combined algorithm can be convergent and agree with that calculated by the FEM very well.

To investigate the influence of the size of the DE subregion on the simulation results the dimension of the DE subregion in the y direction, denoted by w, is changed from 2 mm to 4 mm and 6 mm. The cantilever beam is discretized into 9600 DEs with the radius of 0.5 mm and 19,200 cubic FEs with the size of 1 mm for the combined model in which w equals 4 mm and 14,400 DEs and 14,400 FEs for the combined model in which w equals 6 mm. From the investigation mentioned above the scale factor γ is set to be 0.015 for the three combined models. The deflection at point A on the right free end as shown in Fig. 10 illustrates that the simulation results calculated by the four-point combined algorithm with different sizes of the DE subregions agree with that calculated by the FEM very well.

To study the influence of the size of the discrete and finite elements on the simulation results, the combined model in which w equals 4 mm is discretized into three sets of DEs and FEs with different element sizes. The cantilever beam is discretized into 1200 DEs with the radius of 1.0 mm and 2400 cubic FEs with the size of 2 mm, 9600 DEs with the radius of 0.5 mm and 19,200 cubic FEs with the size of 1 mm, 76,800 DEs with the radius of 0.25 mm and 153,600 cubic FEs with the size of 0.5 mm, respectively. The scale factor γ is set to be 0.015 for the three combined models. Fig. 11 shows the deflection at point A on the right free end. It illustrates that the simulation results calculated by the four-point combined algorithm with different element sizes agree with that calculated by the FEM very well when the size of the element is small enough.

From the studies in this subsection, the four-point combined algorithm can achieve a favorable result when the penalty factor α is set large enough and the size of the element small enough, no

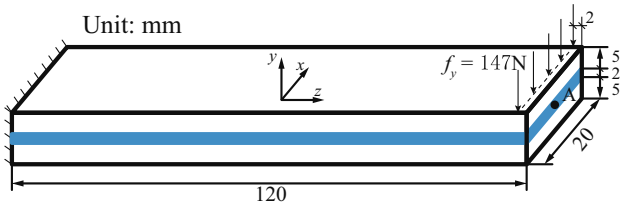

Fig. 7. Cantilever beam under impact load.

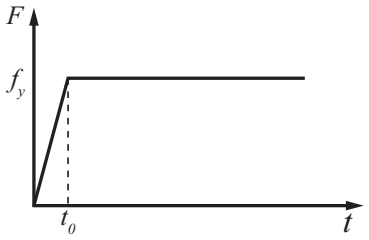

Fig. 8. Impact load acting on the upper surface of the cantilever beam.

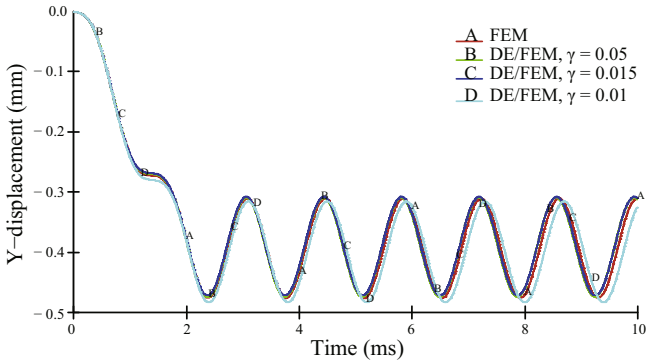

Fig. 9. The deflection at point A on the right free end.

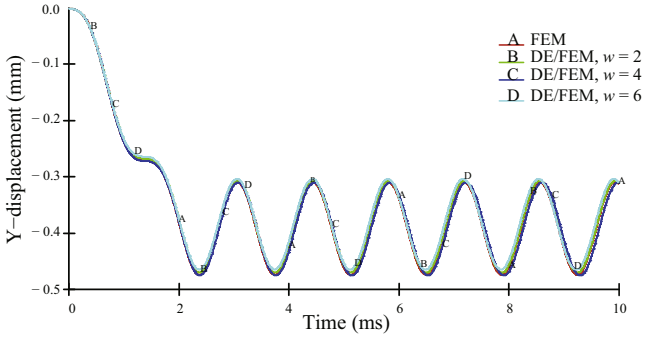

Fig. 10. The deflection at point A on the right free end.

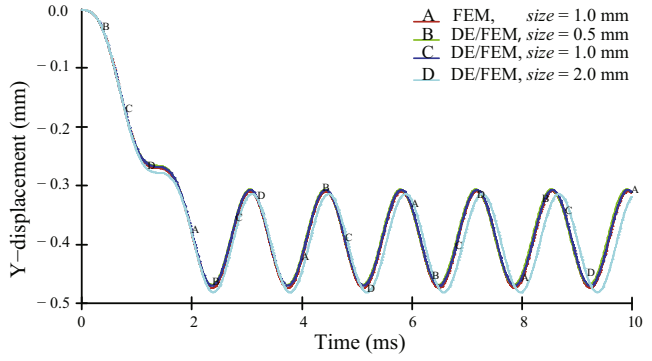

Fig. 11. The deflection at point A on the right free end.

matter whether the size of the DE subregion is small or large. Furthermore the penalty method is conformed by these investigations.

4.2. The impact behavior of the three-point bending glass beam

The excellence of the four-point combined DE/FE algorithm is certified by comparing its simulation results of a three-point bending glass beam with those of the FEM and the surface-center combined DE/FE algorithm (Yu et al., 2010). Subsequently, the validation of the averaged stress tensor is certified by comparing the effective stress (v–m) of the DE with that of the FEM. Then the extrinsic cohesive fracture model is utilized to simulate the impact fracture of the glass beam and the mesh-size dependence is also investigated in the last part of this subsection.

The geometric model of the glass beam is shown in Fig. 12. The initial velocity of the impactor is $V_y = -1.0$ m/s, the size 4 mm × 4 mm × 10 mm and the mass 125 g. The impactor is just on the top of the glass beam. The size of the glass is 200 mm × 20 mm × 10 mm and each support 10 mm × 4 mm × 10 mm. For the combined model, the glass is discretized into 28,000 cubic FEs of the size 1 mm and 12,000 DEs with the radius of 0.5 mm. The whole glass beam model is discretized into 28,220 FEs and 12,000 DEs and the final element configuration of the combined model is illustrated in Fig. 13 which is used to simulate by using the four-point and surface-center combined DE/FE algorithm. The FEM model of the glass beam used to simulate by using the FEM is discretized into 40,220 cubic FEs.

Table 1 lists the material properties of the glass beam. The impactor is considered as rigid body.

Without considering the fracture of the glass beam, the y-displacement curves of the center point at the bottom of the glass beam are calculated by three numerical methods, FEM, four-point and surface-center combined DE/FE algorithm, as shown in Fig. 14. The scale factor γ is set to be 0.013 for both of the combined algorithms. The curve of the four-point combined DE/FE algorithm is almost coincident with that of the FEM, however, the error of surface-center combined DE/FE algorithm comparing with the FEM is larger than that of the four-point combined DE/FE algorithm. For the surface-center combined DE/FE algorithm, a larger scale factor may better the result, which can not reach the precision of the FEM. So the four-point combined DE/FE algorithm is a better alternative to simulate the impact fracture process of the laminated glass later.

The effective stress (v–m) curves of two elements (one DE and one FE just blow the glass beam in the combined model and the FEM model, respectively) are illustrated in Fig. 15. The error of the effective stress of the DE comparing with that of the FE is small enough for engineering problems.

Fig. 16(a) and (b) show the effective stress (v–m) contours of the glass beam at about 0.55 ms and 1.10 ms respectively. The stress distributions simulated by two numerical methods

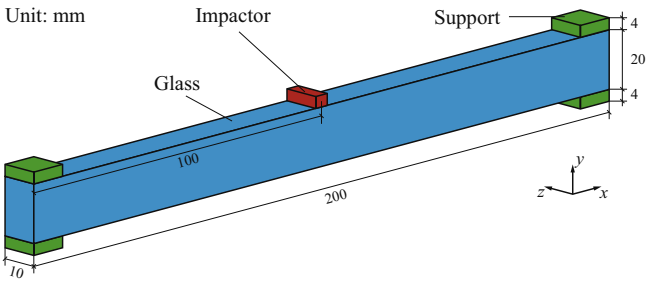

Fig. 12. Three-point bending glass beam.

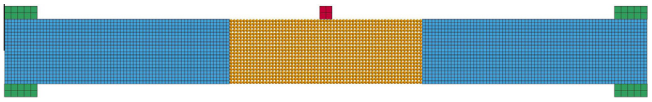

Fig. 13. Element configuration of the combined model.

Table 1
Material properties of the glass beam.

Material	Glass	Support	Impactor
Density ρ (kg/m^3)	2500.0	2400.0	–
Young's modulus E (GPa)	74.09	5.0	210.0
Poisson's ratio v	0.2	0.4	0.269
Tensile strength σ_t (MPa)	100.0	–	–
Energy release rate G_f (N/m)	10.0	–	–

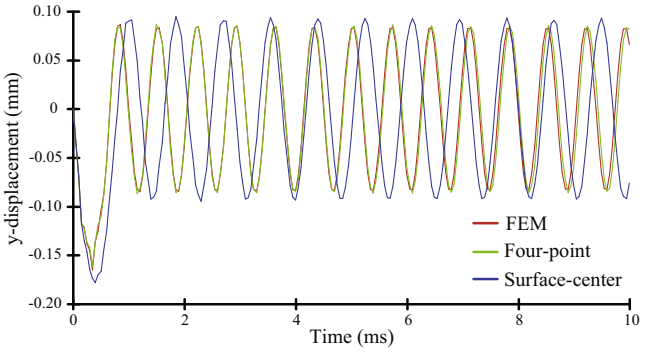

Fig. 14. Y-displacement of the center point on the bottom of the glass beam.

(the FEM and the four-point combined DE/FE algorithm) are similar with each other.

It is obvious that the computational time is greater when using the four-point combined DE/FE algorithm. For the nodal combined DE/FE algorithm the spatial arrangement (Hexahedron layout (Zang et al., 2007; Lei and Zang, 2010)) of DEs was different from those of the others (Cubic layout: Twenty-seven spheres), so the comparison of computational time is proceeding among the last three methods, the surface-center combined method, the freely combined method and the four-point combined method. The simulations of the impact of the glass beam are carried out with a PC. The principal characteristics of the PC are Intel Core i3–370 2.4 GHz (CPU), 2.00 GB (RAM) and Windows 7 Home Basic SP1 32bit (OS). The physics time is set to be 10 ms and the time step 1.2×10^{-4} ms. Fig. 17 illustrates the computational time of the three

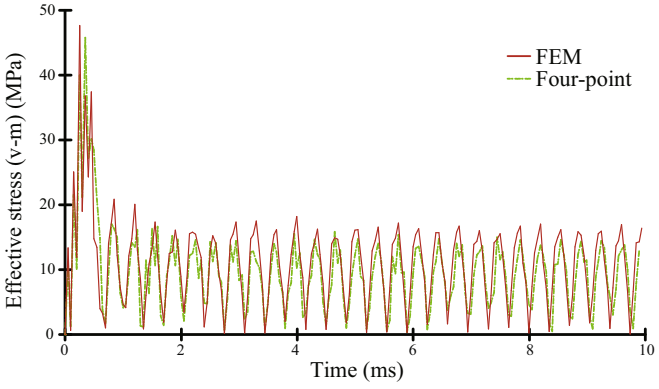

Fig. 15. Effective stress (v–m) of the center point on the bottom of the glass beam.

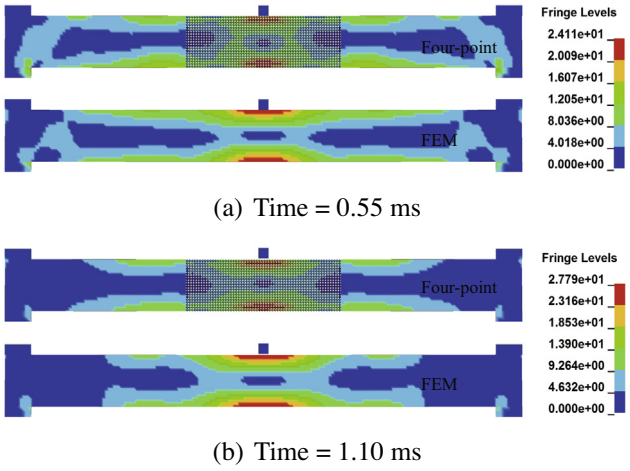

Fig. 16. Effective stress (v–m) contours of the glass beam.

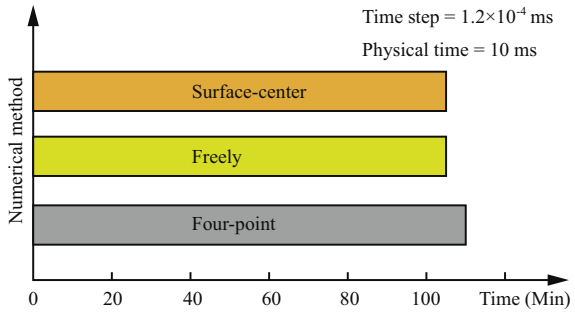

Fig. 17. Computational time of the three combined algorithms.

combined algorithms. The computational time of the surface-center combined method is identical with that of the freely combined method because there is only one linked point for both of them. The efficiency of the four-point combined method has been reduced only 4% compared with the computational time of the both previous methods. The four-point combined method has little effect to reduce the calculation efficiency if the scale of the DEs on the interface is small enough.

Discussion mentioned above shows that the four-point combined DE/FE algorithm is precise enough to calculate the displacement and stress fields in the elastic solid for the impact problems. In order to utilize the four-point combined DE/FE algorithm for the impact fracture of the glass beam and verify the feasibility of the extrinsic cohesive fracture model, the mass of the impactor is changed to be 1 kg with the initial velocity of $v_y = -3.13$ m/s to make sure the impactor have enough kinetic energy to damage the glass beam.

Since the spatial arrangement of the DE has been identified, the mesh dependency of the cohesive model in the DE subdomain is simplified by the size influence on the impact fracture. The DE subdomain as shown in Fig. 13 is discretized by the discrete elements with different radii, r = 1.0 mm, 0.5 mm, respectively. The crack profiles of the glass beam with different element sizes are displayed in Fig. 18. In order to illustrate the damage of the glass the DE's color is set to be red if the joint model of springs between DEs is changed from the connective model to the cohesive or contact model and the main crack is marked by a green line. As shown in Fig. 18(a) one main crack is not propagating completely from the bottom of the glass to the top with the coarse mesh (r = 1.0 mm) at about 130 μs while the fracture reaches the top side of the glass with the fine mesh (r = 0.5 mm). Fig. 18(b) shows the final fracture states at about 300 μs. One main crack is captured in each of them and the cohesive or microcrack zones are distributed around the main cracks. The gap size on the bottom is about 0.70 mm. The size of the cohesive or microcrack zone with the coarse mesh is similar to that with the fine mesh. The distribution of the cohesive or microcrack zones is symmetrical and the main cracks locate in the middle of the glass. The fracture profiles as shown in Fig. 18 indicate the cohesive model in the combined method is mesh-size insensitive and the model with the fine mesh can provide a good resolution for the impact fracture of the glass beam.

Fig. 19 shows the impact fracture history of the glass beam in which one main crack propagates only in the DE subdomain. As shown in Fig. 19(a) the glass beam begins to damage at the bottom at about 57 μs. Subsequently, the main crack progresses upwards in a very short period of time (about 63 μs) to the upper of the glass beam as shown in Fig. 19(a) and the fracture reaches the opposite side at about 120 μs. During the fracture process the joint model of the springs between DEs varies from the connective model to the cohesive or contact model in the surrounding area of main crack and the microcracks and the cohesive zone are located in the red region. Fig. 19(d) illustrates the final fracture state of the three-point bending glass beam at about 300 μs.

The crack location and the crack propagation sequence of the glass beam are identical with the tests in some literatures (Lawn, 1993). So the theory mentioned in this paper can be utilized to simulate the impact fracture process of laminated glass.

4.3. The impact fracture analysis of the laminated glass beam

In this section, the impact fracture process of a laminated glass beam is simulated to compare with the experimental results to verify the effectiveness of the theory in this work.

The impact fracture model of the laminated glass beam is shown in Fig. 20. The laminated glass is suppressed by two outer layers of glass with the size of 200 mm × 10 mm × 10 mm and one piece of PVB interlayer with the size of 200 mm × 4 mm × 10 mm. The four supports and the impactor have the same size as those in Section 4.1. The initial velocity of the impactor is

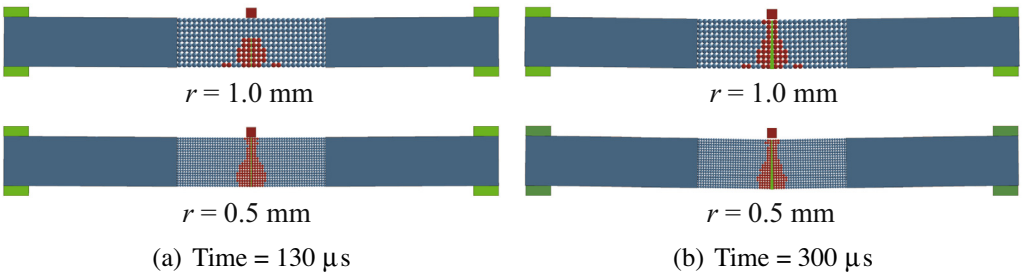

Fig. 18. Cracks profiles with different element sizes.

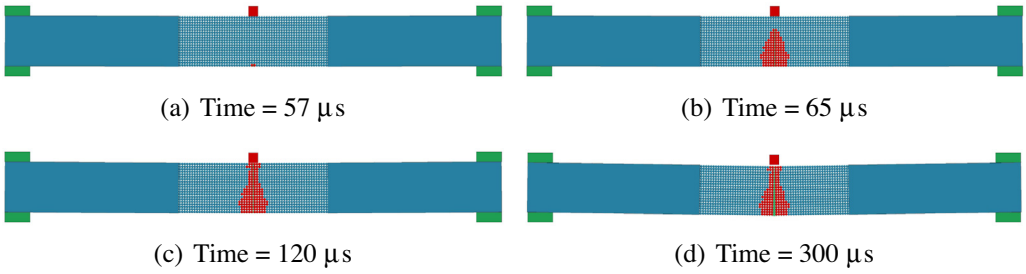

Fig. 19. Impact fracture history of the glass beam.

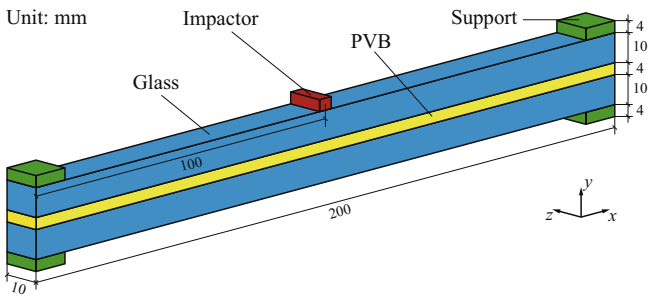

Fig. 20. Impact fracture model of the laminated glass beam.

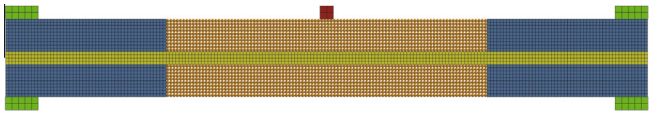

Fig. 21. Element configuration of the laminated glass combined model.

$V_y = -3.13$ m/s and the mass 1 kg. The impactor is just on the top of the laminated glass beam. The geometries of the laminated glass beam are the same as the test pieces (Zang et al., 2009). The material properties of PVB are such that Young's modulus is $E_p = 50.0$ MPa, Poisson's ratio $v_p = 0.48$ and density $\rho_p = 100.0$ kg/m^3. The whole laminated glass beam is discretized into 28,220 cubic FEs and 20,000 DEs and Fig. 21 illustrates the final element configuration of the laminated glass combined model.

Fig. 22 illustrates the impact fracture procedure of the laminated glass beam. The beam begins to damage at the bottom of the upper glass at about 50 μs as shown in Fig. 22(a). Subsequently, the crack progresses upwards in a very short period of time (about 30 μs) in the upper glass and the crack propagates only in the DE subdomain to the top of the upper glass at about 80 μs as shown in Fig. 22(b). After the PVB compressed fully, another main crack begins to propagate upwards in the lower glass at about 205 μs as shown in Fig. 22(c). As time passes, the fracture reaches the opposite side at about 225 μs as shown in Fig. 22(d). Fig. 22(e) shows the final cracks mode at about 500 μs in which there are only two main cracks propagating in the laminated glass beam. During the fracture process there are some microcracks and cohesive DEs in the red surrounding area of the main cracks.

In order to validate the effectiveness of the theory in this paper, the simulation results are compared with the impact failure experimental results of the laminated glass beam (Zang et al., 2009). Fig. 23 shows the photos of two sets of the impact fracture experiments of the laminated glass beam. Time interval of the first set (Fig. 23(a)) was 20 μs and only the crack propagation of the upper glass was recorded. Time interval of the second set (Fig. 23(b)) was 100 μs. The complete fracture process was recorded which included the cracks occurrence and propagation but not detailed. The fracture procedures in the vicinity of the impact point were photographed taking into account the capacity deficiency and small camera angle of the high-speed camera in both sets of experiments. The impact fracture procedure of laminated glass is a very complicated phenomenon. Because of the differences in the production, the experiments conditions and the uniformity of the material, the impact fracture experiments may be different with each other for the laminated glass beams without notches or pre-cracks. Comparing the impact fracture experiments with the simulation results, we notice there are differences in the occurrence of the cracks of the upper and lower glass, but the location of the cracks and the propagation paths are similar to the experimental results. So the theory mentioned in this paper is effective

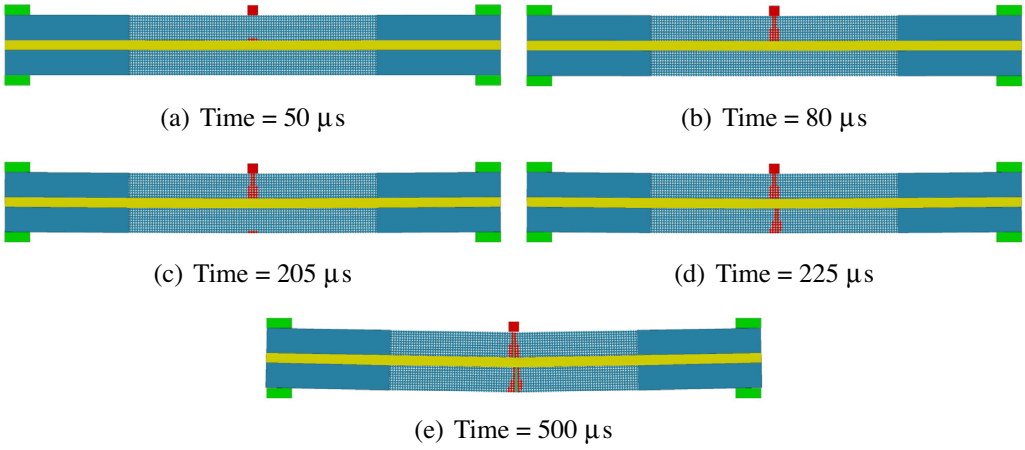

Fig. 22. Fracture procedure of the laminated glass beam.

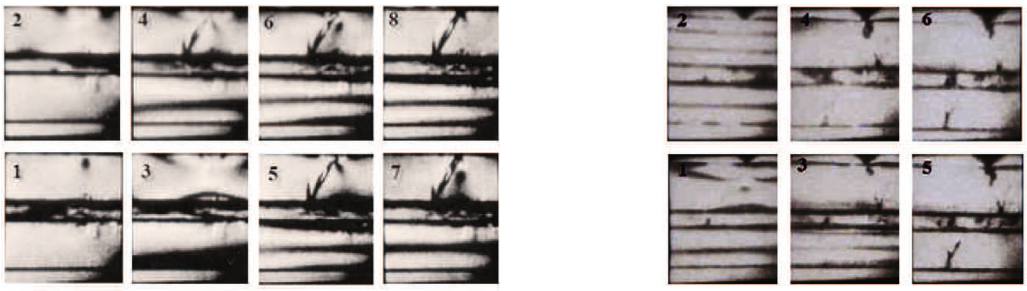

(a) Time interval = 20 μs (b) Time interval = 100 μs

Fig. 23. Impact fracture experiments of the laminated glass beam.

to predict some macroscopic fracture characteristics such as the crack location and crack propagation. In the future this method may be implemented in the study that the automobile laminated windshield subjects to the head impact for the protection of pedestrians safety.

From the discussion mentioned above, we notice the PVB interlayer plays an important role for appeasing the impact load. As shown in Fig. 22(c), the single upper glass brakes into fragments and loses the resistance ability for the impact load, however, there are one main crack begins to progress in the lower glass at about 205 μs. Furthermore, by comparing the whole fracture procedure of the glass beam and that of the laminated glass beam as shown in Fig. 19 (about 63 μs) and Fig. 22 (about 175 μs), we conclude that the PVB interlayer can absorb more energy to temporize the penetration of glass under impact load. When a traffic accident happens, the laminated glass can reduce the probability that heads of passengers may penetrate through the front windshield or any solid flying objects crashing into automobile from outside.

5. Summary

Based on the theory in the paper, the corresponding numerical code has been developed in Fortran 90/95 programming language and the impact behavior of the three-point bending glass beam and the impact fracture procedure of the laminated glass beam are simulated by using the numerical code. From the investigations in this work, the conclusions are summarized as follows:

(1) A four-point combined DE/FE algorithm is proposed to constrain the rotation of the DE about its linked point and analyze the cracks propagation of the laminated glass.
(2) The effectiveness of the four-point combined DE/FE algorithm is validated by comparing the simulation result with those of the FEM and the surface-center combined DE/FE algorithm in the elastic range.
(3) The average stress tensor for granular media is used to an accurate computation of the averaged stress tensor of the DE and its effectiveness is certified by comparing the simulation result with that of the FEM in the elastic range.
(4) The results calculated by using the four-point combined DE/FE algorithm can be convergent as long as the penalty factor is set large enough and the combined method and the cohesive model is mesh-size insensitive.
(5) The impact fracture simulation result of the laminated glass beam is compared with the experimental results to validate the effectiveness of the theory in the paper.

In this work, only the simple crack propagation is simulated. However, considerable more work will be carried out for more complicated impact fracture phenomenon. The size of the cohesive zone will be evaluated quantitatively and the occurrence of microcrack needs more investigation in the future.

Acknowledgements

This work is supported by the National Natural Science Foundation of China (No. 10972079 and 11172104) and the International S&T Cooperation Program of China (No. 2008DFA51740).

References

Choi, J.L., Gethin, D.T., 2009. A discrete finite element modelling and measurements for powder compaction. Model. Simul. Mater. Sci. Eng. 17 (3), 035005.
Cundall, P., 1971. A computer model for simulating progressive largescale movements in blocky rock systems. In: Proceedings, Symposium on International Society for Rock Mechanics, vol. 1, pp. 129-136.
de Saxcé, G., Fortin, J., Millet, O., 2004. About the numerical simulation of the dynamics of granular media and the definition of the mean stress tensor. Mech. Mater. 36, 1175–1184.
Fortin, J., Millet, O., de Saxcé, G., 2003. Construction of an averaged stress tensor for a granular medium. Eur. J. Mech. A/Solids 22 (4), 567–582.
Frenning, G., 2008. An efficient finite/discrete element procedure for simulating compression of 3D particle assemblies. Comput. Methods Appl. Mech. Eng. 197 (49–50), 4266–4272.
Gao, W., Zang, M.Y., 2013. Simulation of impact fracture process of laminated glass beam based on cohesive model. J. South China Univ. Technol. Nat. Sci. 41 (5), 139–144 (in Chinese).
Gao, W., Zang, M.Y., Xu, W., 2014. An approach to freely combining 3D discrete and finite element methods. Int. J. Comput. Methods 11 (1).
Gethin, D.T., Yang, X.S., Lewis, R.W., 2006. A two dimensional combined discrete and finite element scheme for simulating the flow and compaction of systems comprising irregular particulates. Comput. Methods Appl. Mech. Eng. 195 (41–43), 5552–5565.
Karami, A., Stead, D., 2008. Asperity degradation and damage in the direct shear test: a hybrid FEM/DEM approach. Rock Mech. Rock Eng. 41 (2), 229–266.
Komodromos, P., 2005. A simplified updated lagrangian approach for combining discrete and finite element methods. Comput. Mech. 35 (4), 305–313.
Komodromos, P.I., Williams, J.R., 2004. Dynamic simulation of multiple deformable bodies using combined discrete and finite element methods. Eng. Comput. 21 (2–4), 431–448.
Lawn, B., 1993. Fracture of Brittle Solids, second ed. Cambridge University Press, Cambridge, United Kingdom.
Lei, Z., Zang, M.Y., 2010. An approach to combining 3D discrete and finite element methods based on penalty function method. Comput. Mech. 46 (4), 609–619.
Lewis, R.W., Gethin, D.T., Yang, X.S., Rowe, R.C., 2005. A combined finite-discrete element method for simulating pharmaceutical powder tableting. Int. J. Numer. Methods Eng. 62 (7), 853–869.
Munjiza, A., 2004. The Combined Finite-discrete Element Method. John Wiley & Sons Ltd, England.
Munjiza, A., Andrews, K.R.F., 1998. NBS contact detection algorithm for bodies of similar size. Int. J. Numer. Methods Eng. 43 (1), 131–149.
Munjiza, A., Rougier, E., John, N.W.M., 2006. MR linear contact detection algorithm. Int. J. Numer. Methods Eng. 66 (1), 46–71.
Oñate, E., Rojekb, J., 2004. Combination of discrete element and finite element methods for dynamic analysis of geomechanics problems. Comput. Methods Appl. Mech. Eng. 193 (27–29), 3087–3128.
Ortiz, M., Pandolfi, A., 1999. Finite-deformation irreversible cohesive elements for three-dimensional crack-propagation analysis. Int. J. Numer. Methods Eng. 44, 1267–1282.

Sakai, S., Maenaka, K., Kakuda, H. et al, 2013. Optimum design of impact resistance of laminated glass plate. In: 10th World Congress on Structural and Multidisciplinary Optimization, Orlando, Florida, USA.

Shan, L., Ming, C., Liu, K.X., 2009. New discrete element models for three-dimensional impact problems. Chin. Phys. Lett. 26, 120202.

Tang, Z.P., Xu, J.L., 2007. A combined discrete/cylindrical shell finite element multiscale method and its application. Chin. J. Comput. Mech. 24 (5), 591–596 (in Chinese).

Williams, J.R., Perkins, E., Cook, B., 2004. A contact algorithm for partitioning N arbitrary sized objects. Eng. Comput. 21 (2–4), 235–248.

Yong, P., Deck, C., Yang, J.K. et al, 2012. Modeling and validation of windscreen laminated glass behavior during fracture. In: 3rd International Conference on Digital Manufacturing and Automation, pp. 541–544.

Yu, J.B., Liu, X.K., Zang, M.Y., 2010. Impacting response emulation of front windshield based on DEM/FEM coupling. J. Hunan Univ. Nat. Sci. 37 (12), 126–129 (in Chinese).

Zang, M.Y., Lei, Z., Wang, S.F., 2007. Investigation of impact fracture behavior of automobile laminated glass by 3D discrete element method. Comput. Mech. 41 (1), 73–83.

Zang, M.Y., Lei, Z., Oda, J., 2009. Static characteristic and impact fracture behavior of automobile glass. J. Mech. Eng. 45 (2), 268–272 (in Chinese).

Zhang, R., Tang, Z.P., 2010. A multiscale method of time and space by coupling three-dimensional DEM and cylindrical shell FEM. Eng. Mech. 27 (4), 44–50 (in Chinese).

Zhang, Z., Paulino, G.H., Celes, W., 2007. Extrinsic cohesive modelling of dynamic fracture and microbranching instability in brittle materials. Int. J. Numer. Methods Eng. 72, 893–923.

Zienkiewicz, O.C., Taylor, R.L., Zhu, J.Z., 2005. The Finite Element Method: Its Basis and Fundamentals, 6th edition. Butterworth-Heinemann, Oxford.